RESEARCH PAPER

Locoregional Melanoma Therapy by Tissue Adhesive Microneedle Patch-assisted Trans-tumoral Delivery of Anticancer Drug

Junghwan Heo, Eun Young Jeon, Kye Il Joo, and Hyung Joon Cha

Abstract Melanoma is one of the most threatening cancers due to its metastatic capacity and its incidence is recently increasing due to ozone depletion and excessive exposure to ultraviolet. Adjuvant therapy after primary surgical resection is commonly used to prevent tumor recurrence. However, its clinical outcome is not often satisfactory, mainly due to insufficient local accumulation and the systemic toxicity of antitumor drugs. Herein, we reported a self-biodegradable tissue adhesive microneedle (MN) patch for localized and sustained delivery of doxorubicin (DOX) *via* microchannels for melanoma growth inhibition. DOX-loaded MN patches were fabricated by casting bioengineered mussel adhesive protein (MAP) solution containing DOX onto poly (dimethyl siloxane) molds with MN-shaped cavities under backside vacuum. The fabricated MAP-based MN patch enabled effective tissue insertion for fresh and living mice skins as well as firm surface adhesion. Notably, DOX-laden MN (DOX-MN) patch significantly suppressed B16F10 melanoma cell proliferation *in vitro*, while drug-free MN patch did not show any cytotoxicity for both NIH3T3 fibroblasts and B16F10 melanoma cells. In a melanoma-bearing mice model, DOX-MN patch treatment induced greater antitumor efficacy as demonstrated by significant decrease in tumor volume and weight and larger necrotic region compared with intratumoral injection of free DOX. We expect that this strategy can also integrate with other immunomodulators to provide further combinative therapy for effectively eradicating tumors.

Keywords: mussel adhesive protein, tissue adhesive microneedle patch, transdermal delivery, doxorubicin, melanoma treatment

Junghwan Heo[†], Eun Young Jeon[+,†], Hyung Joon Cha[*]
Department of Chemical Engineering, Pohang University of Science and Technology, Pohang 37673, Korea
Tel: +82-54-279-2280; Fax: +82-54-279-5528
E-mail: hjcha@postech.ac.kr

Kye Il Joo
Division of Chemical Engineering and Materials Science, Ewha Womans University, Seoul 03760, Korea

[+]Present address: Department of Dermatology, Columbia University Irving Medical Center, New York, NY 10032, USA

[†]Junghwan Heo and Eun Young Jeon contributed equally to this work.

1. Introduction

Skin cancer incidence is increasing globally due to deterioration of ozone layer and consequent higher exposure to ultraviolet radiation [1]. Among skin cancers, malignant melanoma that arises from melanocytes is the greatest concern because of its propensity to metastasize to other body regions [1-3]. Melanoma has significant adverse effects on life quality including functional morbidity, esthetic, and psychological implications as well as substantial economic burden for treatments [4,5]. Surgery is considered as the primary treatment for early-stage melanoma. However, its efficacy at advanced stage is lower and thus, adjuvant therapies such as radiation, chemotherapy, and immuno-therapy should be followed [6,7]. Promisingly, the combination of immune checkpoint inhibition and small-molecule drug, including doxorubicin (DOX) is ongoing in preclinical and clinical studies to increase immune responses against immune-suppressive tumor microenviron-ments [7-9]. Although DOX can promote immunogenic cell death in tumor cells by enhanced presentation of tumor antigens, the direct use of soluble DOX has shown the risk of cardiotoxicity and insufficient circulatory half-life [10,11]. Thus, there is still the need for development of improved methodology and formulations for DOX delivery.

The skin, as a protective barrier against external stimuli, serves as the immune surveillance system, reducing therapeutic effects of conventional topical drug delivery

systems [12]. Microneedle (MN) technology has been widely explored in transdermal delivery of drugs, vaccines, and genes [13,14]. Polymeric MNs enable effective delivery of therapeutics to the immune cell-rich dermis through reversible microchannels in a painless and less invasive manner. Our previous finding proposed the potential of protein-based MN patches as a novel tissue adhesive bandage under wet and dynamic conditions [15]. Bioengineered mussel adhesive protein (MAP)-based swellable MN patch effectively closed and healed wounds, allowing strong surface adhesion *via* both MAP-inherent adhesive property and swelling-mediated entanglement effect and gradual biodegradation. Moreover, we explored the application of tissue adhesive MN patch system for myocardial infarction alleviation by delivering biofunctional MAP incorporating growth factor-derived therapeutic peptides [16].

MAPs have been discovered as essential materials for marine mussels to securely attach to various surfaces in the underwater conditions [17,18]. Previously, bioengineered MAP was successfully mass-produced in a bacterial system to overcome the limited yield of natural extraction [19,20]. Bioengineered MAP has demonstrated its superior adhesive property, biocompatibility, and biodegradability as well as easy fabrication into various formulations including hydrogels, nanoparticles, and patch, as an ideal tissue adhesive biomaterial [21-25].

In the present work, we proposed DOX-loaded MAP-based MN patch system for regression of melanoma with the aim of providing transdermal and sustained release by both diffusion and enzymatic biodegradation and enhancing local retention of the released drug. MN patch was mainly composed of MAP and hydrophilic hyaluronic acid (HA) to increase water-absorption ability and involved the previously reported dityrosine crosslinking by visible light. DOX-loaded MN (DOX-MN) patch was readily fabricated by casting photocrosslinking solution containing drug onto the female molds under backside vacuum and visible light irradiation. The present work successfully provided *in vitro* and *in vivo* demonstration of the utility of tissue adhesive MN patch for trans-tumoral delivery of DOX to suppress melanoma growth. Based on current findings, further study would involve combined therapy with other immuno-modulators for durable and specific antitumor immune responses.

2. Materials and Methods

2.1. Preparation of bioengineered MAP and water-soluble silk fibroin

Bioengineered MAP was produced and purified from an *Escherichia coli* expression system following previously reported methods [19,20]. In brief, transformed *E. coli* BL21 (DE3) cells (Sigma-Aldrich, St. Louis, MO, USA) that were cultured in 5 L Luria-Bertani (LB; Invitrogen, Carlsbad, CA, USA) medium containing ampicillin (Sigma-Aldrich) were induced by the addition of 1 mM isopropyl-b-D-thiogalactopyranoside (Sigma-Aldrich) for the expression of bioengineered MAP. After centrifugation, the cell pellets were lysed and then the isolated inclusion bodies were used to extract bioengineered MAP using 25% (v/v) acetic acid solution (Sigma-Aldrich). MAP also underwent elimination of lipopolysaccharides and endotoxins by previously described further purification steps for *in vivo* applications [20]. Water-soluble silk fibroin (SF) was prepared by dissolution with neutral salts to weaken intermolecular hydrogen bonds. Cocoons of silkworms (Uljin Farm, Uljin, Korea) was degummed at 100°C for 40 min twice to remove sericin proteins using a mixture of 0.094 g/L sodium oleate and 0.056 g/L sodium carbonated dissolved in distilled water (DW). Resultant SF fibers were fully dried at room temperature and then dissolved in a certain solution containing $CaCl_2:H_2O$:ethanol at a molar ratio of 1:8:2 at 100°C for 20 h. The solution was filtered twice through a MiraCloth (Calbiochem, CA, USA), dialyzed in DW, and then lyophilized. Protein concentration was determined following Bradford assay (Bio-Rad, Hercules, CA, USA) with bovine serum albumin (Promega, Madison, WI, USA) as a standard protein.

2.2. Fabrication of protein-based MN patch

A grayscale lithography technique was utilized to construct a female mold for MN patches [15]. Briefly, 1-mm-thick SU-8 (SU-8 2150; MicroChem Laboratory, Round Rock, TX, USA) was selected as a negative photoresist and underwent spin-coating on a glass wafer followed by baking for 12 h. After hardening, back side of SU-8 layer was placed under UV light (365 nm, 350 mJ/cm^2) through a grayscale photomask. Post exposure baking was performed for another 2 h, slowly raising temperature up to 55°C and cooling to room temperature. Finally, this photoresist was developed with propylene glycol methyl ether acetate (MicroChem Laboratory) for 1 h in an ultrasonic bath, followed by 10 sec of rinsing up with isopropyl alcohol (Sigma-Aldrich). Final female mold could be obtained by casting poly (dimethyl siloxane) (Sylgard 184 PDMS; Dow Corning, Midland, MI, USA) on the constructed SU-8-based master mold. The female mold includes 10 × 10 conical micro-sized cavities with a tip-to-tip distance of 750 μm, a height of 750 μm, and a basal diameter of 250 μm, and a tip radius of under 15 μm.

MAP-based MN patch was fabricated as previously described. Briefly, 0.1 mL of photocrosslinking solution containing 35% (wt/vol) MAP, 15% (wt/vol) HA (100 kDa;

LifeCore, Chaska, MN, USA), 1 mM tris(bipyridine) ruthenium(II) chloride (Ru(II)bpy$_3$$^{2+}$; Sigma-Aldrich), and 30 mM sodium persulfate (SPS; Sigma-Aldrich) was casted onto the PDMS female mold and then kept under backside vacuum at -85 kPa and irradiation of fluorescent light for 12 h to induce the filling of solution into the microcavities and photocrosslinking between tyrosine residues of bioengineered MAP.

To fabricate drug-loaded MN patch, molecules such as doxorubicin hydrochloride (Sigma-Aldrich) and rhodamine B (Sigma-Aldrich) were simply mixed in photocrosslinking solutions. DOX and rhodamine B-loaded MN patches were utilized for *in vitro* and *in vivo* anticancer studies and visualization of punctured tissue sites, respectively. Similarly, SF-based MN patch as a control group for *ex vivo* skin adhesive strength and swelling ratio measurements were fabricated by dispensing a mixture of 70% (wt/vol) SF, 1 mM Ru(II)bpy$_3$$^{2+}$, and 30 mM SPS dissolved in DW on the PDMS molds. All MN patches were observed with a confocal microscope (Leica TCS SP5; Leica Microsystems, Wetzlar, Germany) to sort out the defective patches.

2.3. *In vitro* cytocompatibility test

To evaluate cytocompatibility of MAP-based MN patches, the extracts from MN patches were harvested according to ISO 10993-5 [26]. In brief, MN patches were incubated in Dulbecco's modified Eagle's medium (DMEM; Hyclone, Logan, UT, USA) containing 10% (v/v) fetal bovine serum (FBS; Hyclone) and 1% (v/v) streptomycin (Hyclone) at a ratio of 0.1 g/L at 37°C for 24 h. NIH3T3 fibroblasts were seeded in a well of a 24-well tissue culture plate (Corning, NY, USA) at a cell density of 10^4 cells/well and cultured for 24 h at 37°C and 5% CO_2. The supernatant medium of each well was replaced with MN patch-derived extracts and cells were cultured for another 24, 48, and 72 h. The blank medium and 15% dimethyl sulfoxide (DMSO; Sigma-Aldrich) were used as positive and negative controls, respectively. Cell viability was quantitatively assessed using a Cell Counting Kit-8 assay (CCK-8; Dojindo, Rockville, MD, USA). The results from at least triplicates were averaged.

Furthermore, to visualize cytotoxicity of MAP-based MN patches, live/dead staining (Invitrogen) was performed. NIH3T3 fibroblasts were seeded on the 12 mm cell culture coverslips (SPL Life Sciences, Pocheon, Korea) which was located on each well in a 24-well tissue culture plate at a cell density of 10^4 cells/well, and culture at 37°C and 5% CO_2. After 24 h of incubation, the supernatant medium was replaced with gel extracts and cells were incubated for another 24 h. Live/dead reagents were treated to dye cells, and the images was taken at 10× magnification by the confocal microscope.

2.4. Measurement of swelling ratio

To measure the swelling ratios of MN patches, fully-dried MN patches were weighed before (Wi) and after (Wt) immersion in phosphate buffered saline (PBS) at 37°C. After incubation of 10 min, the swollen MN patches were blotted to remove PBS on the surface and then weighed. The swelling ratio was determined from the following equation:

$$\text{swelling ratio (\%)} = [(Wt-Wi)/Wi] \times 100 \qquad (1)$$

The results from at least four samples were averaged to obtain each measurement.

2.5. Measurement of failure force

To measure the failure force of MNs, uniaxial compression tests were performed with a universal test machine (Instron, Norwood, MA, USA) equipped with a 10 kN load cell [27]. Each MN patch was placed on the lower basal stainless-steel plate, and upper moving steel rod with sensor was applied perpendicularly to the attached patch at a constant speed of 1.2 mm/min. Upon contact with the uppermost tips of MNs, the compressive force started to be recorded and the failure force of MNs was thought as a maximum value just before a decline in the force. The fracture force of each MN was calculated by dividing the maximum force by the number of fractured MNs that was identified by a bright-field microscopy (Leica TCS SP5; Leica Microsystems). The results from five samples were averaged to obtain each measurement.

2.6. *Ex vivo* and *in vivo* mouse skin penetration tests

To demonstrate *ex vivo* skin insertion ability of MAP-based MN patch, rhodamine B-loaded patch was applied onto fresh mouse skin (BALB/c nude mouse; Orient Bio, Seongnam, Korea) by gently pressing its backside with a thumb for 5 min. After insertion, the patch was gently removed in parallel direction to skin layer to detach it. The insertion site was washed with PBS and observed by the bright-field microscopy.

Furthermore, *in vivo* skin penetration capacity of MN patch was investigated. MAP-based MN patch was applied onto mouse skin (5 weeks old BALB/c nude mouse; Orient Bio) in the same way above. After 24 h, punctured skin sections were harvested and fixed in 10% buffered formalin (Sigma-Aldrich). For histological analysis, 7-μm-thick sections were stained with hematoxylin and eosin (H&E) and observed with the bright-field microscope. All animal studies were conducted according to guidelines of national regulations and the approval of the local Institutional Animal Care and Use Committee (POSTECH-2018-0009).

2.7. *Ex vivo* porcine skin wet adhesion test

To examine tissue adhesive strength of MAP-based MN

patch under wet condition, uniaxial 90° pulling-off tests were conducted with a universal testing machine. Porcine skin (Stellen Medical, Saint Paul, MN, USA) as a skin substrate was adhered onto a lower stainless-steel plate using cyanoacrylate glue (3M, Maplewood, MN, USA). For wet adhesion testing, 0.2 mL of PBS was dispensed onto the top surface of the skin. Each sample including MAP- and SF-based MN patches and medical skin sealing tape (SteriStrip; 3M) was bonded to the moving upper rod using a double-sided tape, and then applied to porcine skin with 30 N of preload at a rate of 50 mm/min. After 10 min, the attached samples were pulled off until complete displacement at a speed of 2 mm/min with a 10 kN load cell. The results from at least three triplicates were averaged.

2.8. Drug release study

To profile *in vitro* drug releasing kinetics from MNs, 100 μg of doxorubicin hydrochloride was loaded in a MAP-based MN patch by simply mixing it with photocrosslinking solution. DOX-MN patches were incubated in PBS with or without trypsin of 0.2 mg/mL to simulate *in vivo* conditions at 37°C, 180 rpm, and the supernatant including released drugs was monitored by a fluorescence plate reader (Victor3; Perkin Elmer, Waltham, MA, USA) with with $\lambda_{ex} = 470$ nm and $\lambda_{em} = 585$ nm. The results form at least four samples were averaged.

2.9. *In vitro* anticancer efficacy test

To assess *in vitro* anticancer efficacy, DOX-MN patches were fabricated by loading 10 μg of doxorubicin hydrochloride in 0.1 mL of photocrosslinking solution. Murine melanoma cell line B16F10 was cultured in DMEM containing 10% (v/v) FBS, and 1% (v/v) streptomycin at 37°C and 5% CO_2. B16F10 were seeded per well in a 12-well cell culture plate at a cell density of 10^5 cells/well and cultured for 24 h, and then medium was replaced with fresh one. After 24 h of incubation, a reservoir tank with porous membrane (Transwell; Corning) was installed in each well, and then the DOX-MN patch was placed in the reservoir. This transwell system allowed diffusion of the released drug to the cells in the lower well while preventing MN patches from directly contacting the cells. The cells were cultured for another 24 and 48 h, and the anticancer efficacy of the DOX-MN patch was calculated based on the cell viability determined by CCK-8 assay. Cells cultured with drug-free MN patches were used as a control group. The results from at least triplicates were averaged.

2.10. *In vivo* anticancer efficacy test

Mouse tumor experiments were performed in accordance with guidelines of national regulations and the approval of the local Institutional Animal Care and Use Committee (POSTECH-2018-0009). To build a mouse model bearing melanoma, 10^6 B16F10 cells were suspended in Dulbecco's phosphate-buffered saline (Corning) containing Matrigel (Corning, final concentration = 50% (v/v)) and subcutaneously injected into the flank of 5-week-old BALB/c nude mice (Orient Bio). On day 7 when the volume of tumors reached about 100 mm³, B16F10 tumor-bearing mice were randomly segregated into three groups (5 mice per group) including intratumoral injection of PBS or free DOX solution, and insertion of DOX-MN patches. DOX-MN patches containing 5 mg/kg of doxorubicin hydrochloride or the same volume of drugs-free PBS were treated every five days.

Tumor width (W) and length (L) were measured every two days with an electronic caliper, and the volume of tumors was calculated by following equation:

$$\text{tumor volume} = (L \times W^2) / 2 \tag{2}$$

All survived mice were euthanized on day 12 of post-treatment. For histological analysis, mouse tumors were dissected by a surgical blade, weighed, and finally fixed with 10% buffered formalin. The fixed tumors were embedded in paraffin, followed by cutting into 5 μm-thick sections. The sectioned tissues were stained with H&E and observed by the bright-field microscope.

2.11. Statistical analyses

All experiments were performed independently at least in triplicates, and all data are presented as means ± standard deviation (SD). Significance of differences between data were assessed by Student's *t*-test. The values of $^*p < 0.05$, $^{**}p < 0.01$, and $^{***}p < 0.001$ were determined as statistically significant.

3. Results and Discussion

3.1. Fabrication and cytocompatibility of MAP-based MN patch

For effective delivery of anticancer drug into skin cancer, we designed MAP-based patch having conical shaped MNs with a base diameter of 250 μm and a height of 750 μm that could reach the dermis layer (Fig. 1A). DOX-loaded MAP-based MN patches were fabricated using a previously reported customized backside vacuum chamber and visible light-activated di-tyrosine crosslinking of MAP (Fig. 1B) [15]. In particular, we utilized the mixture of MAP and hydrophilic HA with the aim of increasing swelling property of MNs. It was believed that swellable MNs were essential for both improved interfacial adhesion between MNs and surrounding tissue by mechanical interlocking action and effective release of the encapsulated

drug by diffusion. Bright-field images of the resultant MN patch showed evenly distributed conical MNs with keen tips both from a top view and a side view (Fig. 1C).

To assess biocompatibility of MAP-based MN patch, NIH3T3 fibroblast cells were cultured with the extract of the patch (MN extract) that was obtained by following ISO 10993-5 method [26]. We found that there were no statistical differences in cell viabilities between non-treated and MN extracs-treated groups at different culture time points including 24 and 48 h (Fig. 2A). When normalized to the viability of non-treated cells at 24 h of incubation, the viability of NIH3T3 cells grown in the blank medium
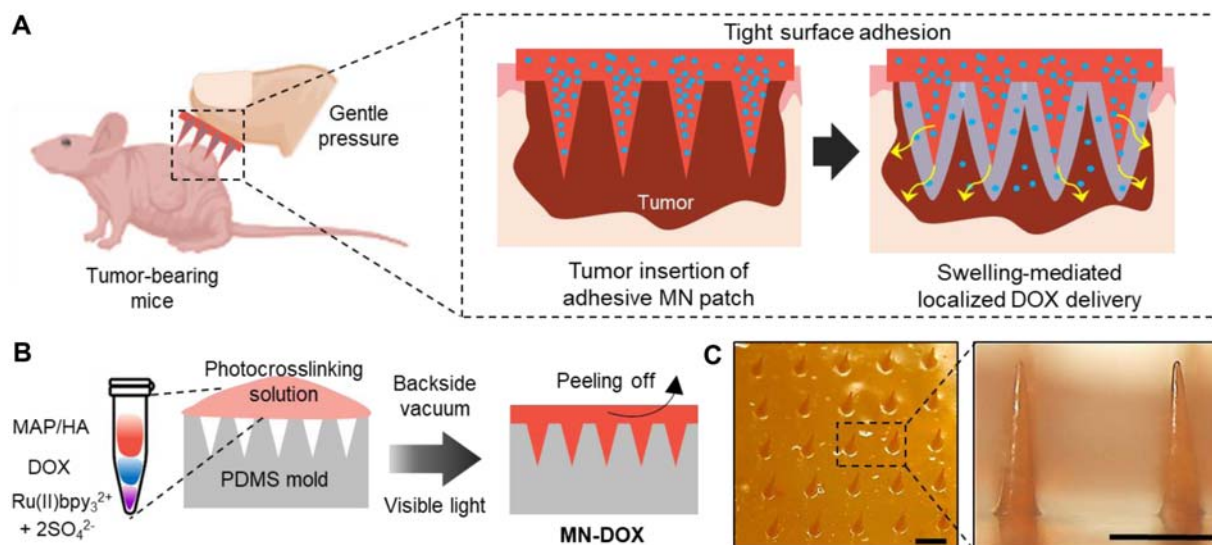

Fig. 1. Fabrication of DOX-loaded MAP-based MN patch for melanoma treatment. (A) Schematic overview showing application of anticancer drug-laden MAP-based MN patch to skin tumor site and its swelling-mediated localized and sustained drug delivery *via* micron-sized holes for effective tumor regression. (B) Schematic illustration of fabrication process of DOX-loaded MAP-based MN patch. Photocrosslinking solution mainly consisting of MAP, HA, and DOX was casting onto the female PDMS mold under backside vacuum chamber and visible light irradiation for dityrosine crosslinking of MAP. (C) Bright-field images of the resultant MAP-based MN patch. Scale bar = 500 μm. DOX: doxorubicin, MAP: mussel adhesive protein, MN: microneedle, HA: hyaluronic acid, PDMS: poly (dimethyl siloxane).
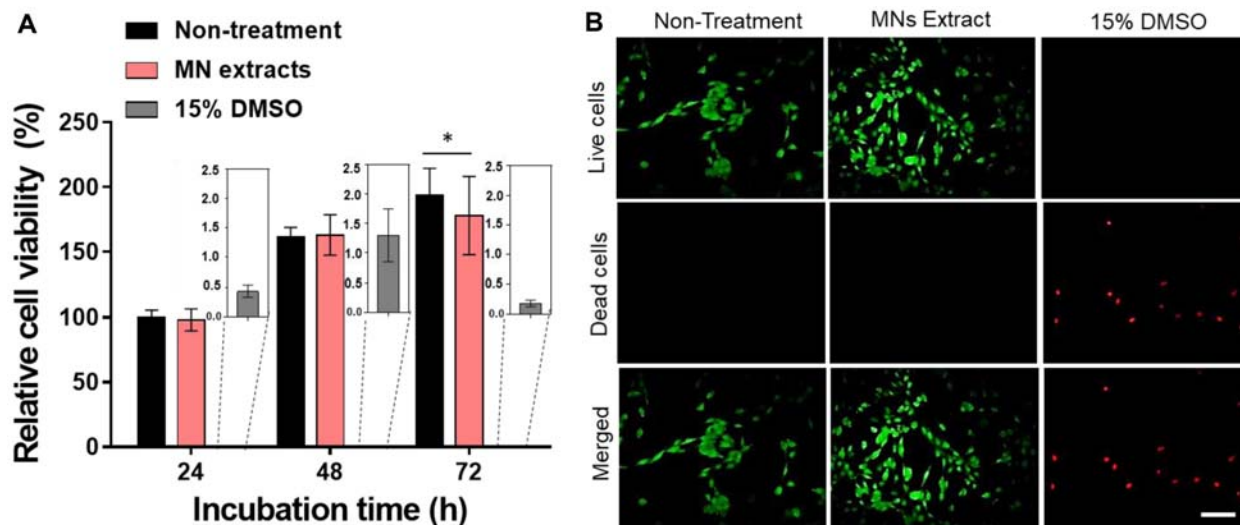

Fig. 2. Cytocompatibility of MAP-based MN patch. (A) Relative viability of NIH3T3 cells cultured with non-treatment, MAP-based MN patch-derived extract (MN extract), and 15% DMSO at 24, 48, and 72 h of incubation (n = 3). Each value was normalized to the viability of non-treated cells at 24 h. (B) Representative images of live/dead staining of non-, MN extract-, and 15% DMSO-treated cells at 24 h of incubation. Scale bar = 100 μm. The values shown are means ± SD. Statistical significance is designated as $^*p < 0.05$. MAP: mussel adhesive protein, MN: microneedle, DMSO: dimethyl sulfoxide.

or medium containing MN extract was $194 \pm 20\%$ and $178 \pm 30\%$, respectively at 72 h, which indicates that cells cultured with MN extract normally proliferated, showing negligible cytotoxic effect. In accordance with cell viability results, live/dead staining of NIH3T3 cells also demonstrated biocompatibility of MAP-based MN patch (Fig. 2B). Red dead cells were rarely detected in non-treated and MN extract-treated groups, whereas most of cells were observed as dead and cell density also decreased a lot due to the detached dead cells in 15% DMSO-treated group.

3.2. Skin penetration and adhesive abilities of MAP-based MN patch

Skin penetration capability of MAP-based MN patch was determined by measurement of the fracture force of MNs. The fracture force was thought to be value when compressive force began to suddenly decline. As shown in Fig. 3A, MAP-based MN patch displayed the average fracture force of 0.42 ± 0.03 N/needle, which was approximately 4-fold stronger than the force required for penetration of fresh

human skin of abdomen region (~0.107 N/needle [28]). Moreover, fresh mouse skin was utilized immediately after animal sacrifice to demonstrate *ex vivo* skin insertion efficiency of MAP-based MN patch (Fig. 3B). Rhodamine B-loaded MN patch having 10×10 MNs was gently applied to mouse skin with a thumb for 5 min, and then slowly detached for observation. The remaining rhodamine B clearly represented punctured tissue sites, which demonstrated ~98% skin insertion efficiency of MNs. Furthermore, to examine *in vivo* skin penetration ability, MAP-based MN patch was applied to the back of the anaesthetized mice in the same way as above, and then punctured skin sections were harvested for H&E staining. Histological examination obviously revealed successful insertion of MNs into the dermis layer as shown by the presence of the remaining tips (Fig. 3C, black arrow). In addition, it was proved that the punctured holes by microneedling were naturally closed without any further damage or infection through tiny holes.

Tight surface adhesion of the patch is necessary to assure effective transdermal delivery of the encapsulated therapeutics
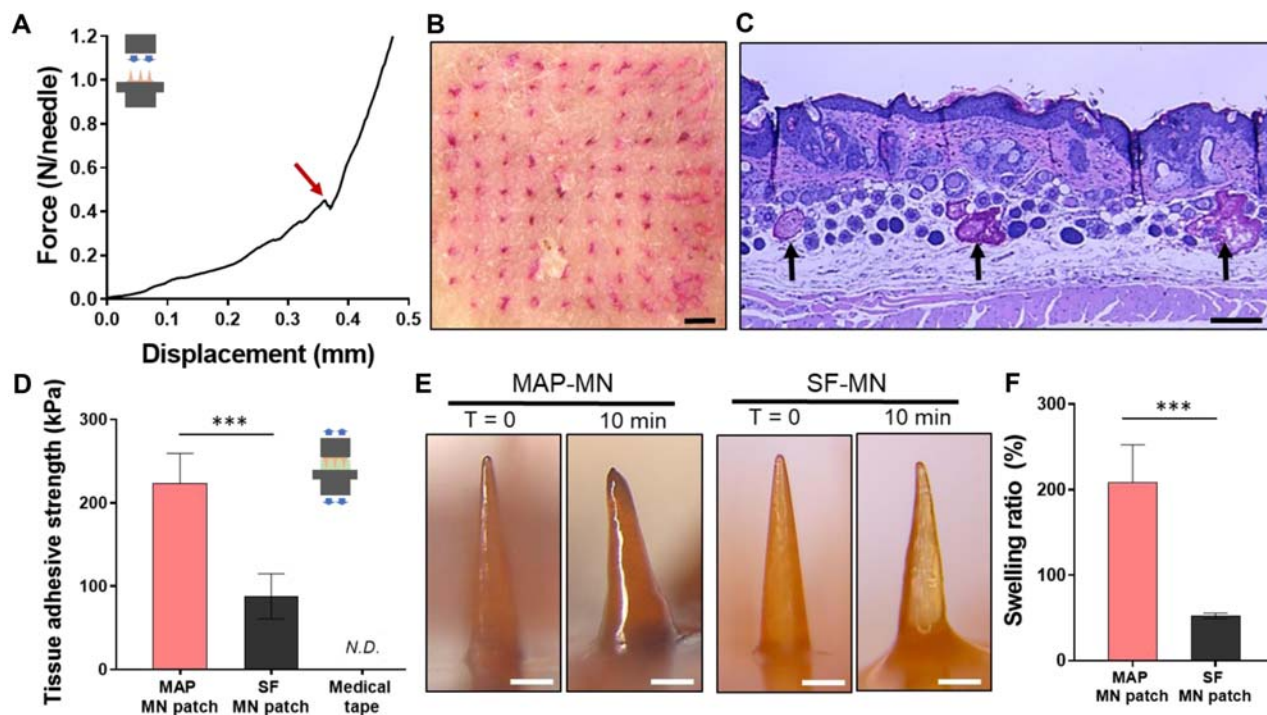

Fig. 3. Characterizations of mechanical properties of MN patch. (A) The curve of compressive force-displacement for MAP-based MN patch to determine the fracture point (indicated by a red arrow). The inset image represents a schematic illustration of the apparatus. (B) Representative bright-field image showing *ex vivo* skin insertion capacity of MAP-based MN patch using fresh mouse skin as a tissue substrate. For visualization of punctured sites, rhodamine B-loaded MN patch was utilized. (C) Representative histological image of vertical sectioned mouse skin after MAP-based MN patch treatment. The black arrows indicate the remaining MNs close to the dermis layer. (D) Measurements of tissue adhesive strengths of MAP- and SF-based MN patches and commercial medical tape on wet surfaces of *ex vivo* porcine skin (n = 3). The inserted image shows the pull-off test setup to measure tissue adhesive strength. (E) Bright-filed images showing swelling behaviors of MAP- and SF-based MNs before and after 10 min of immersion in PBS. (F) Measurement of the swelling ratio of MAP- and SF-based MN patches immersed in PBS (n = 4). Scale bar = (B) 1 mm, (C) 100 μm, and (E) 250 μm. The values shown are means ± SD. Statistical significance is designated as ***$p < 0.001$. MN: microneedle, MAP: mussel adhesive protein, SF: silk fibroin, PBS: phosphate buffered saline, N.D.: not determined.

into the target site. To evaluate tissue adhesive strength of MAP-based MN patch under wet conditions, uniaxial 90° pulling-off tests were performed using fresh porcine skin immersed in PBS (Fig. 3D). Prior to this study, it was found that MAP-based MN patch reached an equilibrium swollen state in 10 min after incubation in PBS (Fig. 3E). Thus, after 10 min of tissue insertion required for gradual swelling of MNs, the attached patch was pulled off until complete displacement to determine maximum strength. As a result, tissue adhesive strength of MAP-based MN patch was 223 ± 36 kPa, while SF-based MN patch as a negative control displayed lower strength of 88 ± 27 kPa and commercial medical tape lost its skin adhesion ability after exposed to wet condition (Fig. 3D). These results suggested that our MAP-based MN patch system could achieve strong tissue adhesion by synergetic actions of swellable MN-driven mechanical entanglement effect and MAP-derived surface adhesion. Indeed, we found that MAP-based MN patch showed radial expansion upon contact with PBS and the swelling ratio of MAP-based MN patch was $208.7 \pm 43.8\%$, which was approximately 4-fold higher than those of SF-based MN patch ($52.4 \pm 3.2\%$) (Fig. 3F). The swollen MNs further could interact with the surrounding tissue through the previously reported MAP-inherent various interactions, leading to improvement in surface adhesion. It has been thought that their characteristic equal amounts of aromatic residues and cationic residues allow diverse interfacial adhesion including cation-π, π-π stacking, electrostatic interaction, hydrophobic interaction, and hydrogen bonding [18,19,29-31]. Collectively, our MAP-based MN patch provides easy and secure application onto the wet surface of skin due to its excellent tissue insertion and adhesive properties.

3.3. *In vitro* drug release profile and anticancer efficacy of DOX-MN patch

To evaluate drug release profile, 100 µg of doxorubicin hydrochloride was loaded in MAP-based MN patch *via* simple mixing before casting onto the mold. The amount of DOX released from the patch was monitored by incubation in PBS or PBS containing 0.02 mg/mL trypsin to mimic physiological environments where proteolytic enzymes are prominent. As shown in Fig. 4A, $70.5 \pm 6.1\%$ of DOX was continuously released from MN patch in the presence of trypsin for 5 days. This gradual and sustained release could be achieved *via* both initial swelling-mediated diffusion and following enzymatic degradation of the swollen MNs. In the case of small molecular drug delivery, steady and controlled release ability is strongly required for improving therapeutic efficacy by minimizing drug loss and side effects resulting from burst release in the initial stage [32-34]. It is also expected that drug release behavior of MAP-based MN patch can be further fine-tuned by adjusting the concentrations of components in photocrosslinking solution for administration of target dose with desirable release speed [21,35].

Moreover, antitumor efficacy of the released DOX was assessed by culturing murine melanoma B16F10 cells with DOX-MN patch. Cell viability was normalized to those of cells cultured with drug-free MN patch. When cultured with DOX-MN patch, the growth of the melanoma cells was highly inhibited, as demonstrated by gradual decrease in the relative cell viability from $54.6 \pm 9.5\%$ at 24 h of culture to $3.0 \pm 2.2\%$ at 48 h (Fig. 4B). This result indicates that the released DOX from MN patch effectively exerted anticancer effect against melanoma cells.
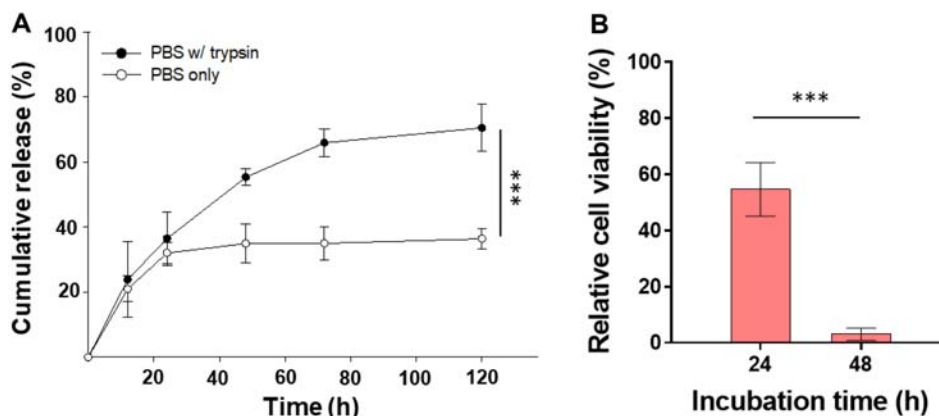

Fig. 4. *In vitro* DOX release profile and anticancer efficacy of DOX-MN patch. (A) Cumulative release of the encapsulated DOX from DOX-MN patch immersed in PBS or PBS containing trypsin (n = 3). (B) *In vitro* anticancer efficacy of DOX-MN patch against B16F10 melanoma cells based on cell viabilities at 24 and 48 h of culture (n = 3). Cell viability was normalized to that of cells cultured with drug-free MAP-based MN patch at each time point. The values shown are means ± SD. Statistical significance is designated as [***]p < 0.001. DOX: doxorubicin, MN: microneedle, PBS: phosphate buffered saline, MAP: mussel adhesive protein.

3.4. *In vivo* evaluation of anticancer efficacy of DOX-MN patch

To investigate *in vivo* anticancer efficacy, DOX-MN patch was applied to the tumor site of BALB/c nu/nu mouse when the tumor reached an average volume of 100 mm³ (Fig. 5A) [36]. PBS or free doxorubicin dissolved in PBS (IT-DOX) were also intratumorally injected into the central region of the tumor as a control group. DOX-MN patch was successfully placed onto the tumor site without any aid of suturing (Fig. 5B). As shown in Fig. 5C, an effective regression of tumor growth was exerted by DOX-MN treatment, while PBS or IT-DOX injection did not suppress tumor growth. At day 12 of treatment, the tumor volume of DOX-MN-treated group was significantly reduced by 29.7% and 46.8% in comparison to the PBS and IT-DOX injections, respectively. Gross observation and weighing of excised

tumors also clearly supported superior anticancer efficacy in those receiving DOX-MN treatment (Fig. 5D and 5E).

Furthermore, H&E-stained tumor sections revealed that in DOX-MN-treated mice, tumors showed large regions of necrosis including both early stage (fragmented and small nucleus) and late stage (ghost cells without nucleus) [24,37,38], indicating that DOX-MN treatment had effects on early and later aspects of cell death (Fig. 5F). In contrast, no necrotic morphology and decrease in nuclear density were observed in PBS- and IT-DOX-injected groups. It would be reasonable assumption that free DOX injection failed to exert durable antitumor efficacy due to fast loss of DOX molecules from the injected site in bodily fluids [39]. To extend the circulation half-life of DOX and its retention at tumor sites, early efforts utilizing poly(ethylene glycol) coating have been extensively studied [40,41]. From this
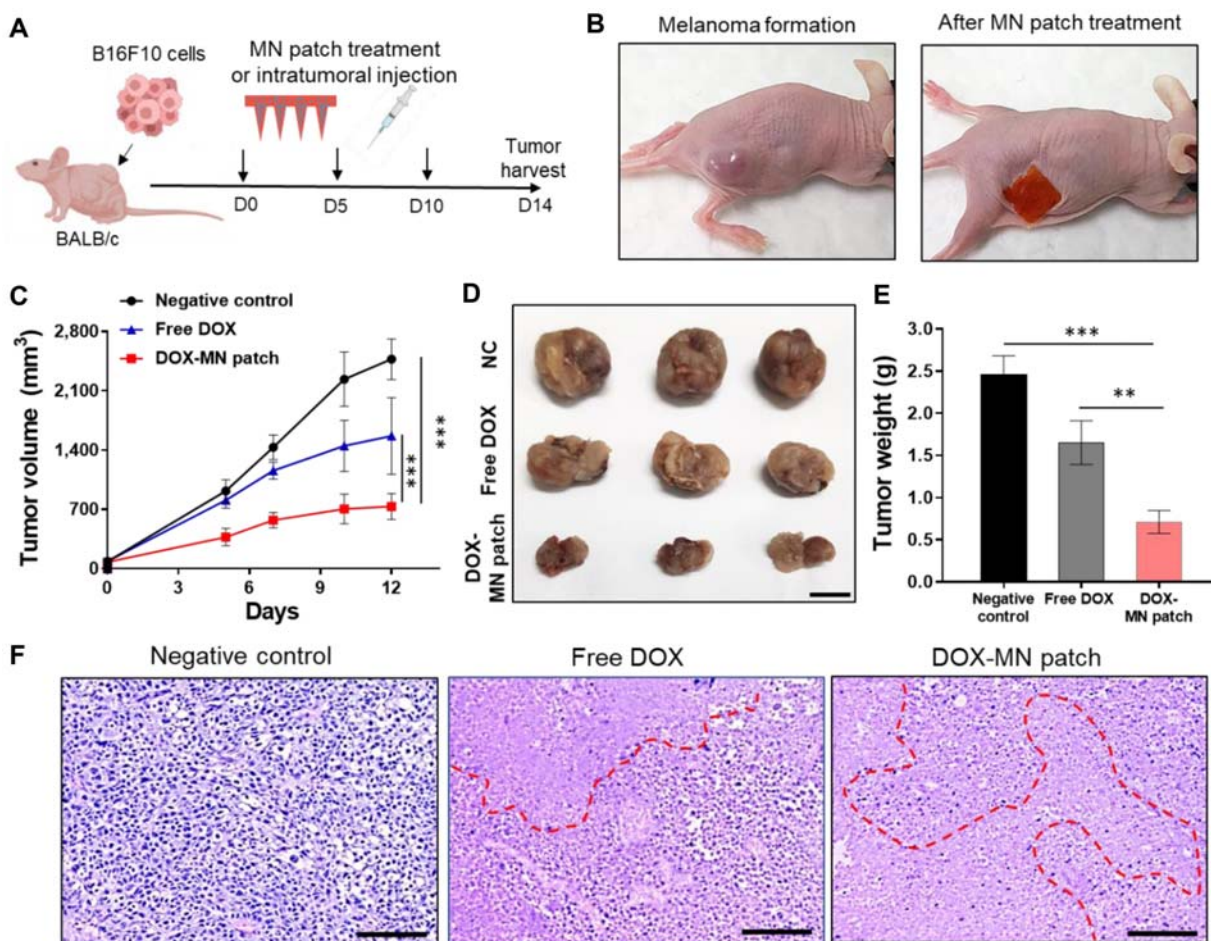

Fig. 5. *In vivo* application and anticancer efficacy of DOX-MN patch in a mouse melanoma model. (A) Schematic illustration showing experimental design: B16F10 melanoma cells were injected subcutaneously into the flank of BALB/c mice at day -7 (n = 5). DOX-MN patch was applied, or PBS and free DOX were intratumorally injected into the tumors at day 0, 5, and 10. (B) Photographs of the tumor-bearing mouse before and after DOX-MN patch treatment. (C) Tumor growth profiles of three different groups for 12 days after treatments. (D) Photographs and (E) measurements of the weights of harvested tumors from three different treatments at day 14. (F) Histological observations of H&E-stained tissues after intratumoral injections of PBS and free DOX, and DOX-MN patch treatments at day 14. Red dashed line indicates the necrotic regions. Scale bar = 100 μm. The values shown are means ± SD. Statistical significance is designated as $^{**}p < 0.01$ and $^{***}p < 0.001$. DOX: doxorubicin, MN: microneedle, PBS: phosphate buffered saline.

aspect, MAP-based MN patch might be beneficial for sustained and localized delivery of the encapsulated DOX through micro-sized channels at tumor site, while assuring tight surface adhesion of the patch to the tumor surface. In particular, the combinative use of MAP and HA as the backbone of MNs might contribute to improved local retention of the released DOX upon dissolution of MNs because of its inherent superior underwater adhesive and water-immiscible properties [23,42-44]. Indeed, our previous studies have demonstrated that injection of MAP/HA-based coacervates into subcutaneous or cardiac infarcted regions potentiated long-term retention of the delivered stem cells at target sites compared to free cell injections [43,44]. Collectively, our proposed DOX-MN patch system achieved the greatest anticancer effects on melanoma growth inhibition *via* localized release of the encapsulated DOX in a simple and convenient way.

4. Conclusion

Transdermal delivery of DOX by tissue adhesive MAP-based MN patch enabled the sustained release and improved antitumor efficacy in mouse skin tumor studies. DOX was easily loaded into MAP-based photocrosslinking solution by simple mixing and fabricated into MN patch under backside vacuum and visible blue light irradiation. These MAP-based MN patch showed sufficient mechanical stiffness to penetrate both intact mouse skin and tumor-bearing mouse skin, strong tissue adhesive strength on wet surface, biocompatibility, and biodegradability. *In vitro* studies demonstrated that the encapsulated DOX could be sustainedly released from water-absorbing MN patch *via* early diffusion and subsequent enzymatic degradation of MAP-based crosslinked backbone. In addition, *in vivo* studies revealed that significant tumor growth inhibition was observed in mice treated with DOX-MN patches and the tumor volume was 46.8% of those of mice that received intratumoral injection of free DOX solution on day 12 of post-treatment. Thus, drug-loaded MAP-based MN patch system is a promising strategy for melanoma treatment as adjuvant therapy to repress tumor recurrence.

Acknowledgements

Author's Contributions

J. Heo: Conceptualization, Validation, Investigation, Writing. E.Y. Jeon: Validation, Methodology, Visualization, Writing. K.I. Joo: Conceptualization, Validation. H.J. Cha: Supervision, Funding acquisition, Resources, Writing.

Ethical Statements

The authors declare no competing financial interests or personal relationships. All animal studies were conducted according to guidelines of national regulations and the approval of the local Institutional Animal Care and Use Committee (POSTECH-2018-0009).

Data Availability

The raw data required to reproduce these findings will be made available upon request.

References

1. Parker, E. R. (2021) The influence of climate change on skin cancer incidence - a review of the evidence. *Int. J. Womens Dermatol.* 7: 17-27. (Erratum published 2021, *Int. J. Womens Dermatol.* 7: 867)

2. Erdmann, F., J. Lortet-Tieulent, J. Schüz, H. Zeeb, R. Greinert, E. W. Breitbart, and F. Bray (2013) International trends in the incidence of malignant melanoma 1953-2008--are recent generations at higher or lower risk? *Int. J. Cancer* 132: 385-400.

3. Naik, P. P. (2021) Cutaneous malignant melanoma: a review of early diagnosis and management. *World J. Oncol.* 12: 7-19.

4. Guy, G. P., Jr., S. R. Machlin, D. U. Ekwueme, and K. R. Yabroff (2015) Prevalence and costs of skin cancer treatment in the U.S., 2002-2006 and 2007-2011. *Am. J. Prev. Med.* 48: 183-187.

5. Sampogna, F., A. Paradisi, M. L. Iemboli, F. Ricci, G. Sonego, and D. Abeni (2019) Comparison of quality of life between melanoma and non-melanoma skin cancer patients. *Eur. J. Dermatol.* 29: 185-191.

6. Miller, K. D., L. Nogueira, A. B. Mariotto, J. H. Rowland, K. R. Yabroff, C. M. Alfano, A. Jemal, J. L. Kramer, and R. L. Siegel (2019) Cancer treatment and survivorship statistics, 2019. *CA Cancer J. Clin.* 69: 363-385.

7. Rios-Doria, J., N. Durham, L. Wetzel, R. Rothstein, J. Chesebrough, N. Holoweckyj, W. Zhao, C. C. Leow, and R. Hollingsworth (2015) Doxil synergizes with cancer immunotherapies to enhance antitumor responses in syngeneic mouse models. *Neoplasia* 17: 661-670.

8. Chitphet, K., S. M. Geary, C. H. Chan, A. L. Simons, G. J. Weiner, and A. K. Salem (2020) Combining doxorubicin-loaded PEGylated poly(lactide-co-glycolide) nanoparticles with checkpoint inhibition safely enhances therapeutic efficacy in a melanoma model. *ACS Biomater. Sci. Eng.* 6: 2659-2667.

9. Riley, R. S., C. H. June, R. Langer, and M. J. Mitchell (2019) Delivery technologies for cancer immunotherapy. *Nat. Rev. Drug Discov.* 18: 175-196.

10. Hershman, D. L., A. Eisenberger, J. Wang, J. Jacobson, V. Grann,

R. McBride, W. Tsai, and A. Neugut (2007) Doxorubicin, cardiac risk factors and cardiac toxicity in elderly patients with diffuse b-cell non-Hodgkin's lymphoma. *J. Clin. Oncol.* 25(18 Suppl): 9050.

11. Renu, K., L. P. Pureti, B. Vellingiri, and A. Valsala Gopalakrishnan (2022) Toxic effects and molecular mechanism of doxorubicin on different organs – an update. *Toxin Rev.* 41: 650-674.

12. Roberts, M. S., H. S. Cheruvu, S. E. Mangion, A. Alinaghi, H. A. Benson, Y. Mohammed, A. Holmes, J. van der Hoek, M. Pastore, and J. E. Grice (2021) Topical drug delivery: history, percutaneous absorption, and product development. *Adv. Drug Deliv. Rev.* 177: 113929.

13. Nagarkar, R., M. Singh, H. X. Nguyen, and S. Jonnalagadda (2020) A review of recent advances in microneedle technology for transdermal drug delivery. *J. Drug Deliv. Sci. Technol.* 59: 101923.

14. Ye, Y., J. Yu, D. Wen, A. R. Kahkoska, and Z. Gu (2018) Polymeric microneedles for transdermal protein delivery. *Adv. Drug Deliv. Rev.* 127: 106-118.

15. Jeon, E. Y., J. Lee, B. J. Kim, K. I. Joo, K. H. Kim, G. Lim, and H. J. Cha (2019) Bio-inspired swellable hydrogel-forming double-layered adhesive microneedle protein patch for regenerative internal/external surgical closure. *Biomaterials* 222: 119439.

16. Lim, S., T. Y. Park, E. Y. Jeon, K. I. Joo, and H. J. Cha (2021) Double-layered adhesive microneedle bandage based on biofunctionalized mussel protein for cardiac tissue regeneration. *Biomaterials* 278: 121171.

17. Waite, J. H. (1987) Nature's underwater adhesive specialist. *Int. J. Adhes. Adhes.* 7: 9-14.

18. Liu, C. (2022) Comparative proteomics for an in-depth understanding of bioadhesion mechanisms and evolution across metazoans. *J. Proteomics* 256: 104506.

19. Hwang, D. S., Y. Gim, H. J. Yoo, and H. J. Cha (2007) Practical recombinant hybrid mussel bioadhesive fp-151. *Biomaterials* 28: 3560-3568.

20. Choi, B.-H., H. Cheong, Y. K. Jo, S. Y. Bahn, J. H. Seo, and H. J. Cha (2014) Highly purified mussel adhesive protein to secure biosafety for *in vivo* applications. *Microb. Cell Fact.* 13: 52.

21. Jeon, E. Y., B. H. Hwang, Y. J. Yang, B. J. Kim, B.-H. Choi, G. Y. Jung, and H. J. Cha (2015) Rapidly light-activated surgical protein glue inspired by mussel adhesion and insect structural crosslinking. *Biomaterials* 67: 11-19.

22. Kim, B. J., D. X. Oh, S. Kim, J. H. Seo, D. S. Hwang, A. Masic, D. K. Han, and H. J. Cha (2014) Mussel-mimetic protein-based adhesive hydrogel. *Biomacromolecules* 15: 1579-1585.

23. Lim, S., Y. S. Choi, D. G. Kang, Y. H. Song, and H. J. Cha (2010) The adhesive properties of coacervated recombinant hybrid mussel adhesive proteins. *Biomaterials* 31: 3715-3722.

24. Jeong, Y., Y. K. Jo, B. J. Kim, B. Yang, K. I. Joo, and H. J. Cha (2018) Sprayable adhesive nanotherapeutics: mussel-protein-based nanoparticles for highly efficient locoregional cancer therapy. *ACS Nano* 12: 8909-8919.

25. Cheong, H., Y.-J. Jun, E. Y. Jeon, J. I. Lee, H. J. Jo, H. Y. Park, E. Kim, J. W. Rhie, K. I. Joo, and H. J. Cha (2022) Sutureless neurorrhaphy system using a macrophage-polarizing *in situ* visible light-crosslinkable adhesive protein hydrogel for functional nerve regeneration. *Chem. Eng. J.* 445: 136641.

26. Wallin, R. F. and E. Arscott (1998) A practical guide to ISO 10993-5: cytotoxicity. *Med. Device Diagn. Ind.* 20: 96-98.

27. Park, J.-H., M. G. Allen, and M. R. Prausnitz (2005) Biodegradable polymer microneedles: fabrication, mechanics and transdermal drug delivery. *J. Control. Release* 104: 51-66.

28. Ranamukhaarachchi, S. A., S. Lehnert, S. L. Ranamukhaarachchi,

29. L. Sprenger, T. Schneider, I. Mansoor, K. Rai, U. Häfeli, and B. Stoeber (2016) A micromechanical comparison of human and porcine skin before and after preservation by freezing for medical device development. *Sci. Rep.* 6: 32074.

29. Lu, Q., E. Danner, J. H. Waite, J. N. Israelachvili, H. Zeng, and D. S. Hwang (2013) Adhesion of mussel foot proteins to different substrate surfaces. *J. R. Soc. Interface* 10: 20120759.

30. Kim, S., A. Faghihnejad, Y. Lee, Y. Jho, H. Zeng, and D. S. Hwang (2015) Cation-π interaction in DOPA-deficient mussel adhesive protein mfp-1. *J. Mater. Chem. B* 3: 738-743.

31. Hwang, D. S., H. Zeng, Q. Lu, J. Israelachvili, and J. H. Waite (2012) Adhesion mechanism in a DOPA-deficient foot protein from green mussels. *Soft Matter* 8: 5640-5648.

32. Tacar, O., P. Sriamornsak, and C. R. Dass (2013) Doxorubicin: an update on anticancer molecular action, toxicity and novel drug delivery systems. *J. Pharm. Pharmacol.* 65: 157-170.

33. Thedrattanawong, C., C. Manaspon, and N. Nasongkla (2018) Controlling the burst release of doxorubicin from polymeric depots via adjusting hydrophobic/hydrophilic properties. *J. Drug Deliv. Sci. Technol.* 46: 446-451.

34. Senapati, S., A. K. Mahanta, S. Kumar, and P. Maiti (2018) Controlled drug delivery vehicles for cancer treatment and their performance. *Signal Transduct. Target. Ther.* 3: 7.

35. Li, J. and D. J. Mooney (2016) Designing hydrogels for controlled drug delivery. *Nat. Rev. Mater.* 1: 16071.

36. de Moura, L. D., L. N. M. Ribeiro, F. V. de Carvalho, G. H. Rodrigues da Silva, P. C. Lima Fernandes, S. Q. Brunetto, C. D. Ramos, L. A. Velloso, D. R. de Araújo, and E. de Paula (2021) Docetaxel and lidocaine co-loaded (NLC-in-hydrogel) hybrid system designed for the treatment of melanoma. *Pharmaceutics* 13: 1552.

37. Debreli Coskun, M., T. Sudha, D. J. Bharali, S. Celikler, P. J. Davis, and S. A. Mousa (2020) αvβ3 integrin antagonists enhance chemotherapy response in an orthotopic pancreatic cancer model. *Front. Pharmacol.* 11: 95.

38. Alyahya, R., T. Sudha, M. Racz, S. C. Stain, and S. A. Mousa (2015) Anti-metastasis efficacy and safety of non-anticoagulant heparin derivative versus low molecular weight heparin in surgical pancreatic cancer models. *Int. J. Oncol.* 46: 1225-1231.

39. Vargason, A. M., A. C. Anselmo, and S. Mitragotri (2021) The evolution of commercial drug delivery technologies. *Nat. Biomed. Eng.* 5: 951-967.

40. Li, L., R. Chen, D. Zhou, J. Sun, L. Wang, L. Zhu, H. Shen, W. Xie, and X. Ye (2022) The efficacy and cardiac toxicity of different-dose pegylated liposomal doxorubicin in elderly patients with diffuse large B lymphoma. *Cancer Med.* Advance online publication. doi: 10.1002/cam4.5280

41. Barenholz, Y. C. (2012) Doxil®--the first FDA-approved nano-drug: lessons learned. *J. Control. Release* 160: 117-134.

42. Kim, H. J., B. Yang, T. Y. Park, S. Lim, and H. J. Cha (2017) Complex coacervates based on recombinant mussel adhesive proteins: their characterization and applications. *Soft Matter* 13: 7704-7716.

43. Park, T. Y., J.-M. Oh, J. S. Cho, S. B. Sim, J. Lee, and H. J. Cha (2020) Stem cell-loaded adhesive immiscible liquid for regeneration of myocardial infarction. *J. Control. Release* 321: 602-615.

44. Park, T. Y., E. Y. Jeon, H. J. Kim, B.-H. Choi, and H. J. Cha (2019) Prolonged cell persistence with enhanced multipotency and rapid angiogenesis of hypoxia pre-conditioned stem cells encapsulated in marine-inspired adhesive and immiscible liquid micro-droplets. *Acta Biomater.* 86: 257-268.